Available online at www.keaipublishing.com/en/journals/journal-of-magnesium-and-alloys/

ScienceDirect

Journal of Magnesium and Alloys 13 (2025) 3740–3750

www.elsevier.com/locate/jma

Full Length Article

Li^+/Mg^{2+} co-intercalation SnS_2-SPAN cathode for super-stable magnesium-based batteries ☆

Yiyi Wang [a], Zhenfeng Guan [a], Yinggan Zhang [a], Baihua Qu [b,c,*], Baisheng Sa [d], Xiaoyuan Zhou [b,c], Jingfeng Wang [b,c], Dong-Liang Peng [a,*], Qingshui Xie [a,*], Fusheng Pan [b,c]

[a] *State Key Lab of Physical Chemistry of Solid Surface, Fujian Key Laboratory of Surface and Interface Engineering for High Performance Materials, College of Materials, Xiamen University, Xiamen, 361005, China*

[b] *College of Materials Science and Engineering, National Engineering Research Center for Magnesium Alloys, Chongqing University, Chongqing, 400044, China*

[c] *Chongqing Institute of New Energy Storage Materials and Equipment, Chongqing, 401135, China*

[d] *Multiscale Computational Materials Facility, College of Materials Science and Engineering, Fuzhou University, Fuzhou, 350100, China*

Received 26 August 2024; received in revised form 5 November 2024; accepted 22 November 2024

Available online 6 December 2024

Abstract

Magnesium-lithium hybrid batteries (MLHBs) have gained increasing attention due to their combined advantages of rapid ion insertion/extraction cathode and magnesium metal anode. Herein, SnS_2-SPAN hybrid cathode with strong C-Sn bond and rich defects is ingeniously constructed to realize Mg^{2+}/Li^+ co-intercalation. The physical and chemical double-confinement synergistic engineering of sulfurized polyacrylonitrile can suppress the agglomeration of SnS_2 nanoparticles and the volume expansion, simultaneously promote charge transfer and enhance structural stability. The introduced abundant sulfur vacancies provide more active sites for Mg^{2+}/Li^+ co-intercalation. Meanwhile, the beneficial effects of rich sulfur defects and C-Sn bond on enhanced electrochemical properties are further evidenced by density-functional theory (DFT) calculations. Therefore, compared with pristine SnS_2, SnS_2-SPAN cathode displays high specific capacity (218 mAh g^{-1} at 0.5 A g^{-1} over 700 cycles) and ultra-long cycling life (101 mAh g^{-1} at 5 A g^{-1} up to 28,000 cycles). And a high energy density of 307 Wh kg^{-1} can be realized by the SnS_2-SPAN//Mg pouch cell. Such elaborate and simple design supplies a reference for the exploitation of advanced cathode materials with excellent electrochemical properties for MLHBs.

Keywords: Dual-confinement host; Rich defects; Co-intercalation; Magnesium-based batteries; Ultralong-cycling lifespan.

1. Introduction

In recent years, the supply risks of lithium resources and safety concerns have undoubtedly been the main hurdles for the long-term development of rechargeable lithium-ion batteries (LIBs) [1–4]. Moreover, univalent Na/K ions with analogous properties to Li^+ also have potential security risks [5,6]. In this case, developing the rechargeable multivalent-ion batteries with higher safety and lower cost has become a hot topic. Compared to LIBs, rechargeable magnesium batteries (RMBs) possesses prominent merits, such as low cost, ultra-high volumetric capacity, and less safety concerns owing to its low dendrite growth propensity [7–11]. These appealing merits have driven RMBs the next "holy grail" in the field of energy storage. However, the sluggish kinetics caused by strong electrostatic interactions between Mg^{2+} and cathode host, along with the incompatibility between electrode materials and electrolytes, lead to the limited cycling life and undesirable reversible capacity, which are detrimental to the

☆ Peer review under the responsibility of Chongqing University.

* Corresponding authors at: State Key Lab of Physical Chemistry of Solid Surface, Fujian Key Laboratory of Surface and Interface Engineering for High Performance Materials, College of Materials, Xiamen University, Xiamen, 361005, China.

E-mail addresses: bhqu@cqu.edu.cn (B. Qu), dlpeng@xmu.edu.cn (D.-L. Peng), xieqsh@xmu.edu.cn (Q. Xie).

https://doi.org/10.1016/j.jma.2024.11.025

exploitation of RMBs [12–16]. There are two effective solutions to solve the above problems. One is to construct a magnesium-lithium hybrid batteries (MLHBs), utilizing Li^+ to assist Mg^{2+} insertion into the host material. The second is to develop advanced cathode materials that can ensure the reversible insertion/extraction of Mg^{2+}.

MLHBs combines the fast ion diffusion of LIBs and high cost efficiency of RMBs [17–21]. Moreover, the growth of Mg dendrites in RMBs is inseparable from electrolyte, especially at large current density, but that can be restrained in MLHBs, which ensure the safety of the cell [19]. Therefore, MLHBs have been appealing in recent years owing to the high specific capacity, high safety and enhanced diffusion kinetics. However, commonly, only Li^+ can intercalate/deintercalate into/from the cathode materials in the majority of MLHBs, limiting their electrochemical performances [17,22]. Given these, designing advanced cathode materials that can simultaneously ensure Mg^{2+}/Li^+ co-intercalation is imperative [20,23].

Several materials have been proposed as cathodes for MLHBs thus far [10,11,15,16,21,24]. Compared to intercalation-type cathode materials, the conversion-alloy type cathode materials have higher theoretical capacities [24–28]. As a typical member of the transition metal dichalcogenides (TMDs), tin disulfide (SnS_2) displays a great potentiality in high-performance MLHBs owing to the large interlayer distance of 0.59 nm and high theoretical capacity [29–32]. For example, Zhao and colleagues rationally designed highly defective SnS_2/HGF composite by utilizing three-dimensional (3D) holey graphene foams (HGF) as a matrix to encapsulate two-dimensional (2D) tin sulfide nanosheets (SnS_2). This composite exhibited satisfactory electrochemical performance as cathode for MLHBs [28]. However, the weak interfacial electrical/chemical coupling between SnS_2 and the carbon matrix is not conducive to the charge transfer, leading to voltage hysteresis and limited cycle life in MLHBs [33,34].

In this work, a SnS_2-SPAN cathode with strong C-Sn bonds and rich defects is proposed and designed for MLHBs. Compared with carbon-based matrices, SPAN matrix can realize the dual-mode confinement of physical barrier and interfacial bounding to SnS_2. Concretely, on the one hand, the SPAN matrix with a good 3D network structure can physically encapsulate SnS_2 nanoparticles and effectively inhibit their agglomeration. On the other hand, the strong interfacial chemical coupling (the formation of C-Sn bond) between SnS_2 and SPAN matrix effectively promotes charge transfer and enhances structural stability. Moreover, abundant sulfur defects provide numerous active sites for the co-intercalation of Li^+ and Mg^{2+} in SnS_2-SPAN with fast kinetics. DFT calculations indicate that the presence of S defects and the formation of C-Sn bond are beneficial for enhancing the adsorption and reducing the diffusion barrier of Li^+ and Mg^{2+} on the SnS_2-SPAN. Additionally, the conversion-alloy and Mg^{2+}/Li^+ co-intercalation mechanisms have been certified in SnS_2-SPAN electrode. As expected, the SnS_2-SPAN cathode with the Li^+/Mg^{2+} co-intercalation displays greatly enhanced structural stability and reaction reversibility. The constructed pouch cell exhibits an energy density up to 307 Wh kg^{-1}.

2. Results and discussion

2.1. Structural characterization

Fig. 1a shows the synthesis of SnS_2-SPAN, which includes two steps, namely, electrospinning firstly and then sulfurization calcination (the detailed preparation procedure is shown in the experimental section). The morphological features of the samples are observed by the scanning electron microscopy (SEM). As contrast sample, SPAN has the staggered "reticular structure" by nanofibers (Fig. S1a-b), which is propitious to stabilizing the SnS_2 nanocrystals and shorting ion diffusion path. While the pure SnS_2 exhibits the irregular flake-like structure and self-aggregates together (Fig. S1c-d). Interestingly, the SnS_2-SPAN composite exhibits a uniform nanofiber morphology with a smooth surface and an average diameter of 200 nm (Fig. 1b-c). The SnS_2 nanocrystals are well-confined in the SPAN matrix, which can be confirmed by the darker region in the TEM images (Fig. 1d). High-resolution TEM image in Fig. 1e clearly displays a d-spacing of 0.59 nm correlated with the (001) face of SnS_2 [31,35]. Meanwhile, the enriched sulfur defects can be discerned clearly, which can effectively facilitate charge transfer and adsorption of guest ions (Li^+ and Mg^{2+}) [28,36]. The element mappings of SnS_2-SPAN sample (Fig. 1f) validate that C, N, S and Sn elements display homogeneous distribution throughout the whole sample, indicating that SnS_2 nanocrystals are well encapsulated in nanofibers.

The phase purity of the SnS_2-SPAN, SPAN and pure SnS_2 samples are identified via X-ray diffraction (XRD) patterns in Fig. 1g. Obviously, all diffraction peaks of the SnS_2-SPAN and SnS_2 samples are well indexed to hexagonal SnS_2 (JCPDS: 023–0677), exhibiting the high purity and crystallinity [32]. A broad peak at 25° in SPAN sample is consistent with the formation of SPAN, which stems from the emergence of sulfur inducing the dehydrogenation reaction of PAN [37–39]. Notably, the peaks of SnS_2-SPAN broaden obviously in comparison with SnS_2, indicating its smaller crystallite size. Generally, the appropriate reduction of crystallite size is helpful to increase the structural stability and specific surface area of the active material, which can shorten the ion diffusion path and provide more active sites for ions insertion/extraction, finally improving the electrochemical performance. Raman spectroscopy is a forceful evidence for attesting the co-existence of SnS_2 and SPAN. As plotted in Fig. 1h, for SPAN sample, a series of peaks at 178 cm^{-1} (C-S), 311 cm^{-1} (C-S), 375 cm^{-1} (C-S), 477 cm^{-1} (S-S), 802 cm^{-1} (C = N), 939 cm^{-1} (S-S) verify the presence of SPAN [38]. Meanwhile, peaks at 1324 cm^{-1} and 1552 cm^{-1} are pertaining to the D and G bands, respectively [26,40]. Except for the characteristic peak at 312 cm^{-1} related to the A_{1g} mode of SnS_2, other characteristic peaks of SnS_2-SPAN sample are consistent with those of SPAN [32]. As expected, only a peak is detected in the Raman spectra of pure SnS_2 sample (Fig.

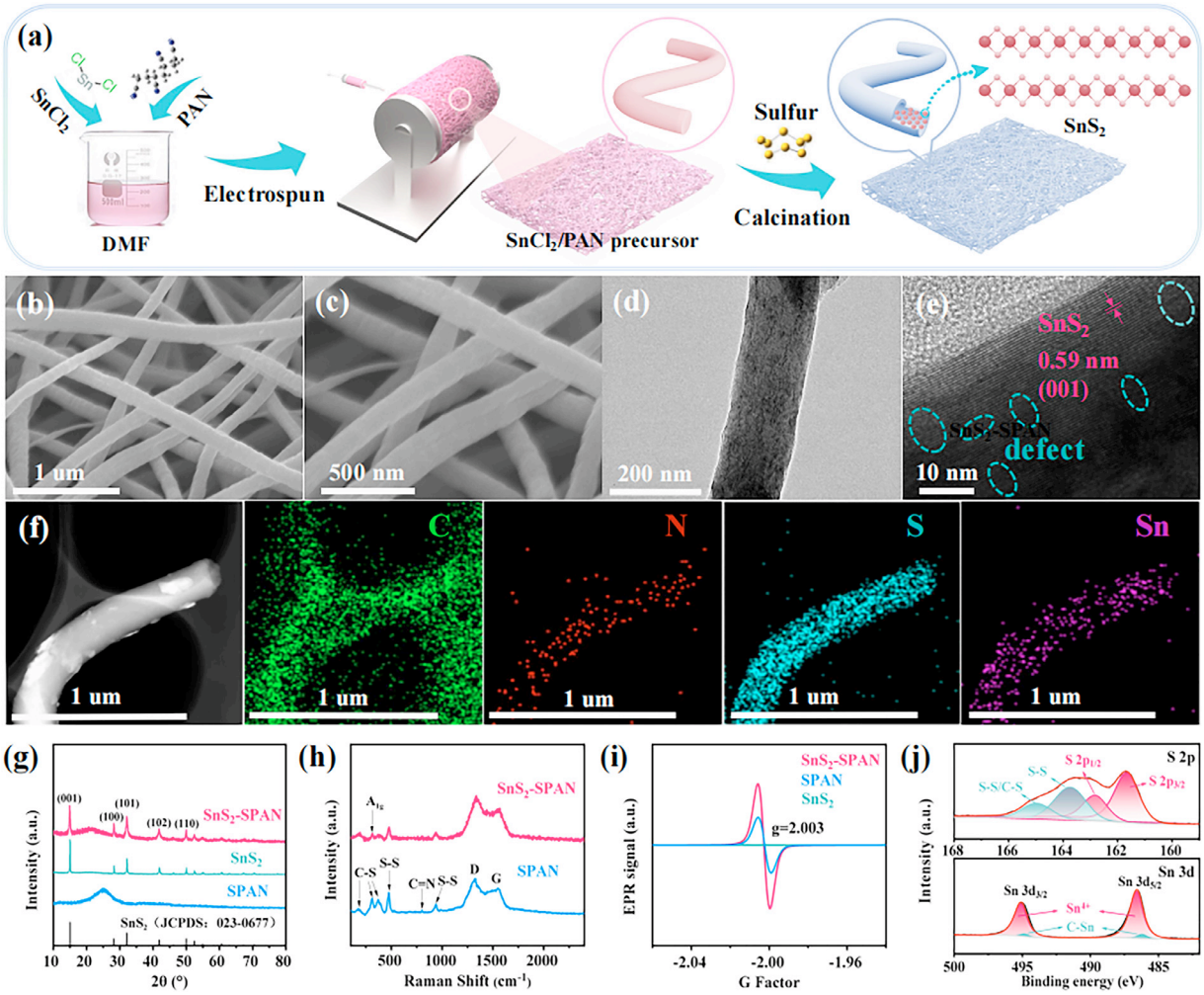

Fig. 1. (a) Schematic illustration to fabricate the SnS_2-SPAN sample. (b, c) SEM, (d) TEM, (e) HRTEM images and (f) corresponding elemental mappings of SnS_2-SPAN sample. (g) XRD patterns, (h) Raman spectra and (i) EPR spectra of SnS_2-SPAN, SnS_2 and SPAN samples. (j) High-resolution S 2p and Sn 3d XPS spectra for SnS_2-SPAN sample.

S2), corresponding to the A_{1g} mode of SnS_2 [31]. Fourier transform infrared (FTIR) spectra are shown in Fig. S3, the appearance of C = C, C–C, C = N, C-S and S-S bonds in the FTIR spectroscopy of SnS_2-SPAN and SPAN samples indicates the successful formation of SPAN [38,41]. Electron paramagnetic resonance (EPR) spectra in Fig. 1i reveal that a noticeable peak (g = 2.003) can be found in the SnS_2-SPAN sample, which showing explicitly higher intensity than that of SPAN and SnS_2 (enlarged view are shown in Fig. S4), indicating the abundant sulfur defect in SnS_2-SPAN composite [36,42,43]. This feature endows SnS_2-SPAN cathode materials with adequate active sites, consequently being conductive to the rapid Li^+/Mg^{2+} co-intercalation. Furthermore, the results of TGA analysis (Fig. S5) show that the weight ratio of SnS_2 in SnS_2-SPAN composite is approximately 37 wt% (the detailed calculation process is shown in supplementary information). Fig. S6 indicates that the specific surface areas of the SnS_2-SPAN, SnS_2 and SPAN samples are 18.0, 12.7 and 8.9 $m^2\ g^{-1}$, respectively. Generally, a relatively large specific surface area and porous structure are conducive to the interfacial contact between the electrolyte and electrode material, which can supply more active sites for the storage of Li^+ and Mg^{2+} [25]. Therefore, compared with SnS_2 and SPAN, it is expected that SnS_2-SPAN can preferably promote the transmission of electrons and guest ions (validated by the subsequent experiments), which is favorable to achieving the superior electrochemical performances.

The SnS_2-SPAN was subjected to X-ray photoelectron spectroscopy (XPS) for analyzing its surface states. It can be seen from Fig. S7a that peaks can be labeled as Sn, S, C and N elements. For S 2p XPS spectrum of SnS_2-SPAN (Fig. 1j), two peaks positioned at 165.0 and 163.7 eV are derived from S–S/C–S and S–S bonds, respectively [41]. Another a pair of peaks at 162.8 and 161.7 eV are pertinent to the S $2p_{1/2}$ and S $2p_{3/2}$, respectively [44]. In Sn 3d XPS spectrum (Fig. 1j), a pair of peaks at 495.1 and 486.6 eV belong to the Sn $3d_{3/2}$ and Sn $3d_{5/2}$ of Sn^{4+}, respectively, accompanied by a pair of inconspicuous peaks at 494.8 and 486.2 eV that are assignable to the C–Sn bond derived from the powerful interface coupling between SPAN and SnS_2, which is beneficial

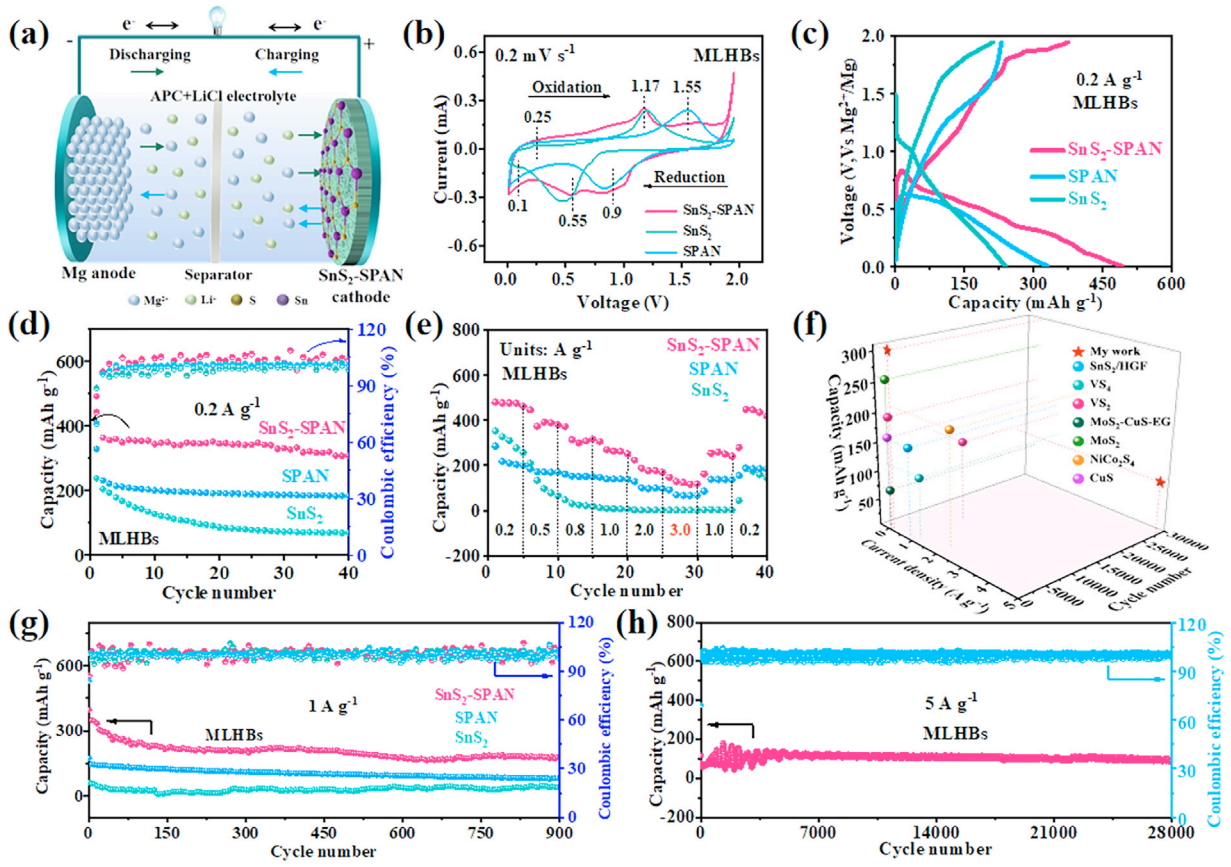

Fig. 2. Electrochemical performances for MLHBs: (a) the schematic diagram of the movement of Li^+/Mg^{2+} during cycling. (b) The 3rd CV curves of all electrodes at 0.2 mV s^{-1}. (c) The initial discharge-charge voltage profiles of SnS_2-SPAN, SnS_2 and SPAN at 0.2 A g^{-1}. (d) Cycling performance at 0.2 A g^{-1} and (e) rate capability of SnS_2-SPAN, SnS_2 and SPAN. (f) Cycling performance metrics comparison of SnS_2-SPAN and previously reported other materials for MLHBs. (g) Long-term cycling performance of SnS_2-SPAN, SnS_2 and SPAN at 1 A g^{-1}. (h) Long-term cycling performance of SnS_2-SPAN at 5 A g^{-1}.

for accelerating charge transfer and ensuring the high stability of structure [32,42,45]. Similarly, as presented in Fig. S7b, the C–Sn bond appears in the C 1 s XPS spectrum, and the C = N, C–N/C-S and C–C/C = C bonds are located at 286.5, 285.8 and 284.8 eV, respectively [32,41]. Typically fitted N 1s XPS spectrum (Fig. S7c) shows the peaks of pyrrolic-N and pyridinic-N, around at 398.3 and 400 eV, respectively [46,47]. These results indicate that the SnS_2-SPAN with strong C-Sn interaction and abundant defects is successfully synthesized.

2.2. Electrochemical performance

The electrochemical properties of the SnS_2-SPAN, SPAN and SnS_2 cathodes in MLHBs and RMBs were systematically evaluated by assembling 2032-type coin cells. Taking SnS_2-SPAN cathode as an example, the schematic diagrams of the movement of guest ions in MLHBs and RMBs during charge and discharge processes are shown in Fig. 2a and Fig. S8, respectively. The storage mechanism and electrochemical kinetics were studied via testing cyclic voltammetry (CV) curves of all electrodes within 0.01–1.95 V, as summarized in Fig. S9. Intuitively, the low current density in RMBs suggests the sluggish mobility of Mg^{2+}, while the redox peaks are more prominent in MLHBs, indicating that the kinetics has been significantly improved, further confirming that the co-insertion of Li^+ could accelerate the reaction kinetics [17,48]. Meanwhile, whether in MLHBs or RMBs, the area of CV curve for SnS_2-SPAN is explicitly larger than that of the SnS_2 and SPAN, further validating faster reaction kinetics and then enhanced specific capacity. Moreover, compared with the CV curves of SPAN in MLHBs (Fig. S9e) and RMBs (Fig. S9f), it is found that SPAN is almost electrochemically inactive for Mg^{2+}. Fig. 2b shows the 3rd CV curves of all electrodes in MLHBs, it is found that the SnS_2-SPAN electrode follows the conversion-alloy mechanism, moreover, SPAN is mainly involved in the reaction at high potential while SnS_2 is mainly involved in the reaction at low potential. Concretely, the reduction peak at around 0.9 V is associated with the conversion reaction between SPAN and Li^+ [49]. Another reduction peak appeared at 0.55 V is related to the conversion reaction between SnS_2 and Mg^{2+}/Li^+, while an unobtrusive peak at 0.1 V is associated with the Sn-Mg alloying reaction [28]. Notably, the Sn-Li alloying reaction can be excluded in MLHBs because it usually occurs between 0.1 and 0.5 V and the redox potential of Li^+/Li is lower than that of Mg^{2+}/Mg [50]. In the charging process, an unobtrusive peak at 0.25 V corresponds to the Sn-Mg de-alloying reaction. Additional two oxidation peaks at around 1.17 and 1.55 V are attributed to

the reversible conversion reaction, involving in the reformation of SnS_2 and SPAN, respectively. The potential difference of redox peaks of SnS_2-SPAN is smaller than that of SnS_2 and SPAN electrodes, demonstrates its smaller polarization and faster reaction kinetics.

The initial galvanostatic charge-discharge profiles (GCD) of three electrodes at 0.2 A g^{-1} in MLHBs are depicted in Fig. 2c. Obviously, the initial (dis)-charge capacities of SnS_2-SPAN electrode are far higher than that of SnS_2 and SPAN. And the voltage gap of charge-discharge curves of SnS_2-SPAN is slightly decreased compared to that of SnS_2 and SPAN, manifesting its reduced polarization, which is consistent with the CV results [51,52]. Fig. S10 shows the GCD of all electrodes in MLHBs and RMBs at 1st, 2nd and 40th cycles, the GCD curve of MLHBs shows the relatively obvious platform while the voltage distribution of RMBs decreases sharply, and the specific capacities of MLHBs are far superior to RMBs, attesting again the significant advantages of Li^+/Mg^{2+} co-insertion. Notably, compared with the rapid capacity fading of SnS_2 (Fig. S10b), the capacities decay of SnS_2-SPAN electrodes is suppressed (Fig. S10a), which is due to the introduction of SPAN that plays a physical and chemical double confinement effects. On the one hand, SPAN with a good 3D network structure can effectively inhibit the agglomeration of SnS_2 and alleviate the volume expansion during charge and discharge processes. On the other hand, the C–Sn chemical bond formed between SnS_2 and SPAN can enhance the interface stability of the material and electron transfer [32,33]. Moreover, as seen from Fig. S10f, the SPAN electrode has almost no capacity, indicating that SPAN is almost electrochemically inactive for Mg^{2+}, which is concordance with the CV result (Fig. S9f). Consequently, when SnS_2-SPAN is applied as the cathode of RMBs, the capacity provided by SPAN is negligible [48,53].

The high discharge capacity and long cycle performances of SnS_2-SPAN in MLHBs and RMBs are concretely evaluated. As illustrated in Fig. 2d, the SnS_2-SPAN electrode shows relatively high initial discharge capacity of 493 mAh g^{-1} at 0.2 A g^{-1} in MLHBs, and a discharge specific capacity of 309 mAh g^{-1} can be persevered after cycling 40 times with relatively stable Coulombic efficiency during cycling, clearly surpassing that of SPAN (184 mAh g^{-1}) and SnS_2 (71 mAh g^{-1}) electrodes. In contrast, the initial discharge capacity of SnS_2-SPAN at 0.2 A g^{-1} in RMBs is about 105 mAh g^{-1} and slightly enhances to 115 mAh g^{-1} after 40 cycles (Fig. S11), much higher than those of SnS_2 (45 mAh g^{-1}) and SPAN (close to zero), suggesting the Mg^{2+} can reversibly insert/extract into/from the SnS_2-SPAN. At 0.5 A g^{-1}, the SnS_2-SPAN electrode can deliver a discharge specific capacities of 218 mAh g^{-1} in MLHBs (Fig. S12a) and 57 mAh g^{-1} in RMBs (Fig. S12b) after cycling 700 times, obviously superior to SnS_2 and SPAN. For comparison, the electrochemical performances of SnS_2-SPAN were also simply tested at 0.5 A g^{-1} in LIBs. In which, the 0.8–2.75 V is selected as the test voltage range, owing to the redox potential difference between Li^+/Li and Mg^{2+}/Mg is 0.67 V [17,28,53]. From Fig. S13a, the discharge specific capacity largely reduces from 62 mAh g^{-1} in 1st cycle to 14 mAh g^{-1} in 700th cycle. The corresponding GCD curve are shown in Fig. S13b.

In addition to high specific capacity, SnS_2-SPAN also exhibits outstanding long-cycle performances in MLHBs and RMBs. After (dis)-charging 900 cycles at 1 A g^{-1} (Fig. 2g), SnS_2-SPAN delivers a high discharge specific capacity of 181 mAh g^{-1} in MLHBs, outperforming those of SPAN (80 mAh g^{-1}) and SnS_2 (42 mAh g^{-1}). Furthermore, the SnS_2-SPAN exhibits an unexpectedly long-term cycling stability even cycled at 5 A g^{-1}. As displayed in Fig. 2h, the capacity has a strong fluctuation at the initial stage and then becomes gradually stable, and a reversible capacity of 101 mAh g^{-1} can be maintained after 28,000 cycles with a CE of ~100%, showing the high reversibility and structural stability. The capacity fluctuations of SnS_2-SPAN electrode can be related to the activation process [23,27,48]. Even in RMBs (Fig. S14), the reversible capacity and corresponding CE of SnS_2-SPAN electrode can retain 23 mAh g^{-1} and ~ 100% after nearly 5900 cycles. The above results indicate that, on the one hand, the physical confinement of SPAN effectively inhibits the agglomeration of SnS_2 nanoparticles, on the other hand, the chemical bonding between SPAN and SnS_2 (the formation of C-Sn bond) enhances the structural stability. Therefore, the SnS_2-SPAN electrode exhibits outstanding electrochemical performances.

Rate capabilities of all electrode for MLHBs and RMBs were tested at gradually enhanced current density. In RMBs (Fig. S15), the specific capacities of SnS_2-SPAN are 104, 53 and 23 mAh g^{-1} at 0.2, 0.5 and 1 A g^{-1}, respectively, confirming the Mg^{2+} can reversibly insert/extract into/from the SnS_2-SPAN at small density current, while the extraction of Mg^{2+} in SnS_2-SPAN is unsatisfactory due to a strong polarization at large current density. Interestingly, as demonstrated in Fig. 2e, the specific capacities of SnS_2-SPAN electrode in MLHBs can reach 318, 252 and 170 mAh g^{-1} at the current densities of 0.8, 1.0 and 2.0 A g^{-1}, respectively. The value can still retain as high as 118 mAh g^{-1} even at 3 A g^{-1}, and the specific capacity can recover to 419 mAh g^{-1} as the current rate recovers to 0.2 A g^{-1}. The above results indicate that the co-intercalation of Li^+ can accelerate the insertion amount of Mg^{2+} into the SnS_2-SPAN owing to a "cooperative effect" between Mg^{2+} and Li^+ [22]. From Fig. 2e and Figure S15, SnS_2-SPAN shows better rate capability than the SnS_2 and SPAN. The decrease of particle size of SnS_2-SPAN is beneficial to shorten the ion diffusion path and improve the reaction kinetics, and the C-Sn bond formed between SnS_2 and SPAN can accelerate charge transfer and ensure high stability of structure, accounting for the improved rate performance of SnS_2-SPAN [42,45]. The corresponding GCD curves of each electrode at gradually enhanced current density (from 0.2 to 3 A g^{-1}) are demonstrated in Fig. S16.

The above results indicate that the electrochemical performances of MLHBs are significantly superior to those of RMBs. This may be due to the synergistic effect between Mg^{2+} and Li^+, where the co-intercalation of Li^+ is beneficial for promoting the intercalation of Mg^{2+}. Moreover, the

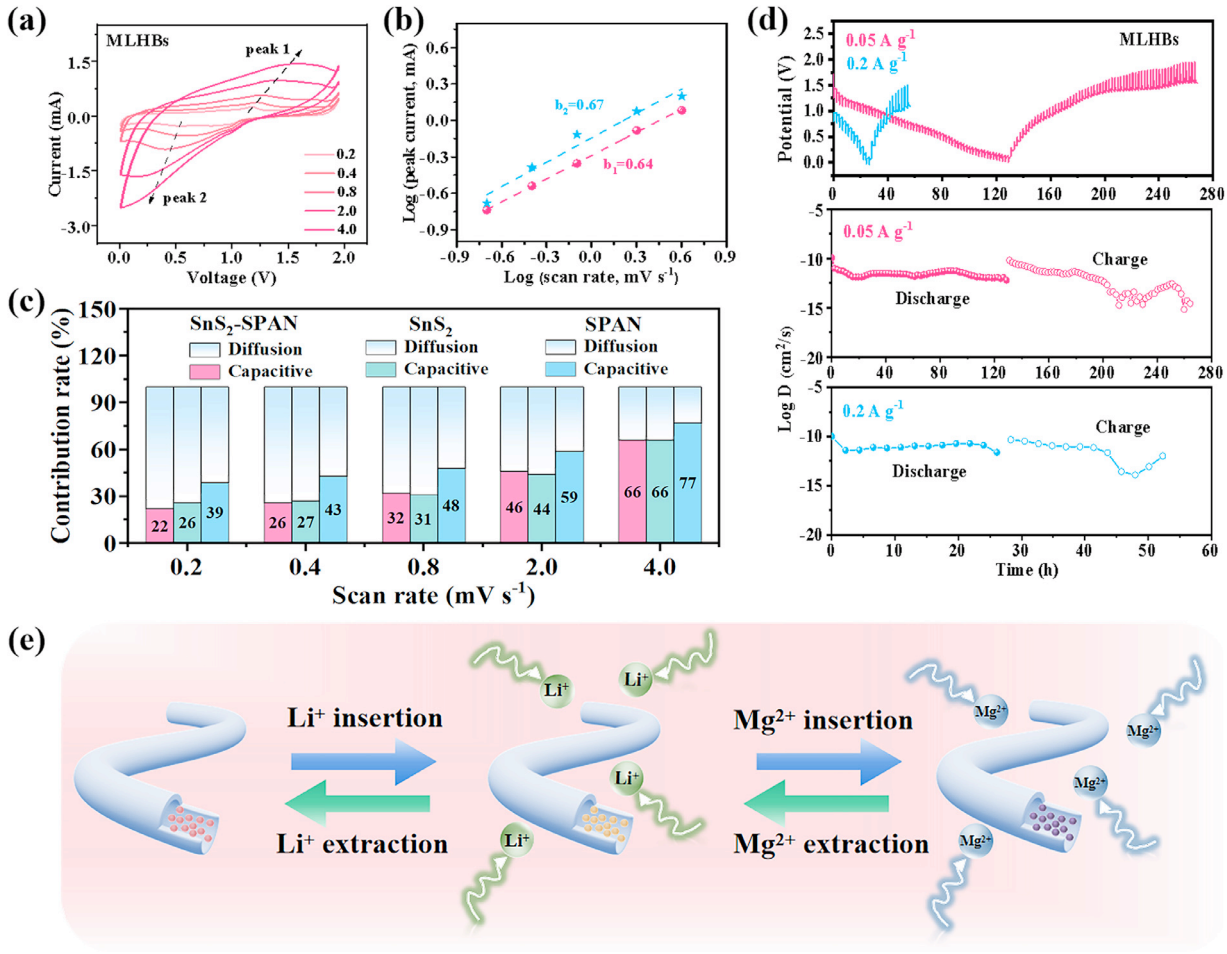

Fig. 3. (a) CV curves at different scan rates and (b) log *i*-log *v* curves of SnS_2-SPAN in MLHBs. (c) Capacitive and diffusion contribution ratio at various scan rates of SnS_2-SPAN, SnS_2 and SPAN in MLHBs. (d) GITT curves and corresponding ion diffusion coefficient of SnS_2-SPAN at 50 and 200 mA g^{-1} in MLHBs. (e) A schematic diagram of Li^+/Mg^{2+} insertion/extraction into/from SnS_2-SPAN.

outstanding electrochemical properties of SnS_2-SPAN is inextricably linked to the double confinement effect of SPAN matrix and rich sulfur defects. Firstly, the robust 3D reticular structure of SPAN can physically confine the aggregation of SnS_2 and mitigate strong volume fluctuations. Secondly, the C–Sn chemical bond formed between SnS_2 and SPAN can effectively enhance the interface stability and electron transport. Finally, the abundant S defects can provide additional ion migration channels and accelerate ion transport [36,43]. Therefore, the SnS_2-SPAN electrode exhibits one of the most superior electrochemical performances among the existing advanced cathodes for MLHBs (Fig. 2f, Fig. S17 and Table S1-S2) [54–58].

2.3. Reaction kinetics analysis

For further elucidating the redox kinetics and reversibility of all cathodes in MLHBs and RMBs, the CV profiles at gradually enhanced scan rates (from 0.2 to 4 mV s^{-1}) were recorded. In MLHBs, the CV profiles of SnS_2-SPAN are displayed in Fig. 3a, the identical shape and the well-defined redox peaks are still preserved in all CV curves, implying the preferable rate capability [59]. However, the voltage gap between reduction peak and oxidation peak increases as the scan rate enhances, suggesting the increased electrochemical polarization. This polarization phenomenon also occurs in the CV curves of SnS_2 and SPAN (Fig. S18a and 18c). Subsequently, whether the electrochemical process is dominated by diffusion-controlled or capacitance-controlled can be judged by the *b* value, which can be acquired by fitting with log(*i*) and log(*v*) in accordance with the following two equations [60–62]:

$$i(v) = av^b$$

$$log(i) = log(a) + blog(v)$$

The *b* value approaches to 0.5 or 1, which means the diffusion-controlled or pseudo-capacitance control is dominant, separately [61]. *b* values of oxidation peak 1 and reduction peak 2 are 0.64 and 0.67 (Fig. 3b), implying the electrochemical process of SnS_2-SPAN cathode is dominated by diffusion process. The results of Fig. S18b and Fig. S18d confirm that the SnS_2 and SPAN also exhibit a dominant diffusion-controlled process, in which the *b* values of peak 1

and peak 2 are 0.59 and 0.67 for SnS_2, and that of peak 1 and peak 2 are 0.69 and 0.74 for SPAN, respectively. Moreover, the capacitive contribution ratio can be obtained according to the following equation [63–65]:

$$i = k_1 v + k_2 v^{1/2}$$

Where the $k_1 v$ stands for the capacitive contribution ratio, $k_2 v^{1/2}$ represents the diffusion-controlled contribution ratio [63]. As seen from Fig. 3c, the capacitive contribution ratio incrementally increases as the scan rate constantly enhances. In RMBs, the CV curves of SnS_2-SPAN, SnS_2 and SPAN at constantly enhanced sweep rates are presented in Fig. S19a-c. Briefly, the shape of all the CV profiles remains basically unchanged as the sweep rate continues to increase. As shown in Fig. S19d-f, the capacitance contribution ratio gradually enhances with the scanning rate increases, those are 89%, 50% and 64% for SnS_2-SPAN, SnS_2 and SPAN at 4 mV s^{-1}, respectively.

Subsequently, the ion diffusion coefficient is obtained by the galvanostatic intermittent titration technique (GITT) test (Fig. S20), aiming to identify the rapid kinetics of working ions (Mg^{2+}/Li^+) in SnS_2-SPAN [22,25]. As presented in Fig. 3d, at 0.05 A g^{-1}, the D value of SnS_2-SPAN fluctuates between 10^{-9} to 10^{-12} cm^2 s^{-1} in the whole discharge process while the average diffusion coefficient D value is 10^{-12} cm^2 s^{-1} in the charge process, revealing a prominent D value and effective working ion fluidity [59]. Moreover, the GITT curves measured at relatively large current density (0.2 A g^{-1}) still display small potential gaps and prominent diffusion coefficient, uncovering the small ohmic polarization [66]. The GITT curves and corresponding ion diffusion coefficient of SnS_2 are shown in Fig. S21. Additionally, the electrochemical impedance spectroscopy (EIS) is conducted to compare charge transfer kinetics of SnS_2-SPAN, SnS_2 and SPAN before and after cycling 50 times in MLHBs and RMBs. As illustrated in Fig. S22, undoubtedly, the resistance for MLHBs is reduced significantly in comparison with RMBs, furthermore, the resistance of SnS_2-SPAN is smaller than that of SnS_2 and SPAN before and after cycling. The superior ion diffusion coefficient and charge transfer kinetics of SnS_2-SPAN electrode can be attributed to the C–Sn bond formed between SnS_2 and SPAN, which promotes the rapid transfer of electrons/ions [53,67]. Fig. 3e displays the schematic diagram of Li^+/Mg^{2+} insertion/extraction into/from SnS_2-SPAN, the preferential insertion of Li^+ can effectively promote the insertion of Mg^{2+}.

2.4. Electrochemical reaction mechanism

A series of in/ex-situ characterizations, including TEM, XRD, Raman and XPS tests were conducted to further clarify the electrochemical reaction mechanism of SnS_2-SPAN in MLHBs. After discharging (Fig. S23a) and charging (Fig. S23d) 50 cycles, SnS_2-SPAN cathode retains original fibrous morphology without significant changes, and preferable fiber morphology after cycling can also be observed from the TEM image (Fig. S23b and Fig. S23e), confirming its excellent structural stability. In Fig. 4a, after one loop, the HRTEM image of discharged SnS_2-SPAN cathode displays d-spacing of 0.31 and 0.33 nm, which are correlated with the (023) face of Mg_2Sn and the (111) face of Li_2S, respectively, confirming the conversion-alloy reaction mechanism. And when charging back to 1.95 V, the HRTEM image (Fig. 4b) shows lattice spacing of 0.32 nm, which is pertinent to the (100) face of the SnS_2, suggesting the excellent reversibility of electrochemical reaction [28]. Additionally, the Mg element was detected in both discharged (Fig. S23c) and charged (Fig. S23f) SnS_2-SPAN cathodes, showing that Mg^{2+} is successfully intercalated into the SnS_2-SPAN host but some Mg^{2+} are still captured in the host after charging, which can be further confirmed by ex-situ XPS and the inductively coupled plasma optical emission spectroscopy (ICP-OES) tests. Fig. S24 shows the XPS spectra of the 1st and 5th cycle at different electrochemical states. For Mg 2p and Li 1s spectra (Fig. 4c), the peaks of Mg 2p and Li 1s are detected after (dis)-charging compared with the pristine electrode, confirming the co-insertion/extraction of Mg^{2+} and Li^+ into/from the SnS_2-SPAN. There is still a part of Mg^{2+} and Li^+ remaining in cathode without extraction after first cycling, and only a small amount of Mg^{2+} and Li^+ remain in the lattice after cycling 5 times. ICP-OES results also confirm the relatively low irreversibility. Specifically, the contents of Li and Mg in the SnS_2-SPAN electrode are 0.64 and 0.60 after discharging to 0.01 V, and there are still 0.17 Li^+ and 0.15 Mg^{2+} remaining in the host after charging back to 1.95 V. The EDS result after cycling (Fig. S25) is consistent with the ICP-OES result. Moreover, in the XPS spectrum of S 2p (Fig. S26), compared with the pristine SnS_2-SPAN cathode, upon discharging to 0.01 V, the peak intensities of the S^{2-} and C–S/S–S significantly weaken owing to the insertion of guest ions. Meanwhile, four pair of new peaks appear, which can be assigned to the Li–S, Mg–S and SO_x, separately [68–70]. In which, the appearance of SO_x may be related to the decomposition of THF solvent. After charging back to 1.95 V, the peak intensity of Mg–S and Li–S are obviously weakened, that of S^{2-} is obviously increased, certifying the reversible reactions.

Ex-situ XRD is also applied to further confirm the conversion-alloy mechanism and the reversibility of the electrochemical reactions. Fig. 4d displays the GCD curves under different electrochemical states at 0.2 A g^{-1}. For pristine electrode, the cathode material is mainly composed of SnS_2 phase besides the strong diffraction peaks at 43.5°, 50.5° and 74.2° related to the Cu current collector [11,23,44,52,65]. When discharging to state I, the diffraction peaks of SnS_2 phase gradually weaken, and the peak at about 15° shifts to lower angle, indicating that ion intercalation leads to crystal structure expansion. In addition, the Li_2S, MgS and Sn phase are formed, indicating the occurrence of conversion reaction. Sequentially discharging to 0.01 V (state II), a diffraction peak correlated with the Mg_2Sn phase appears, indicating the

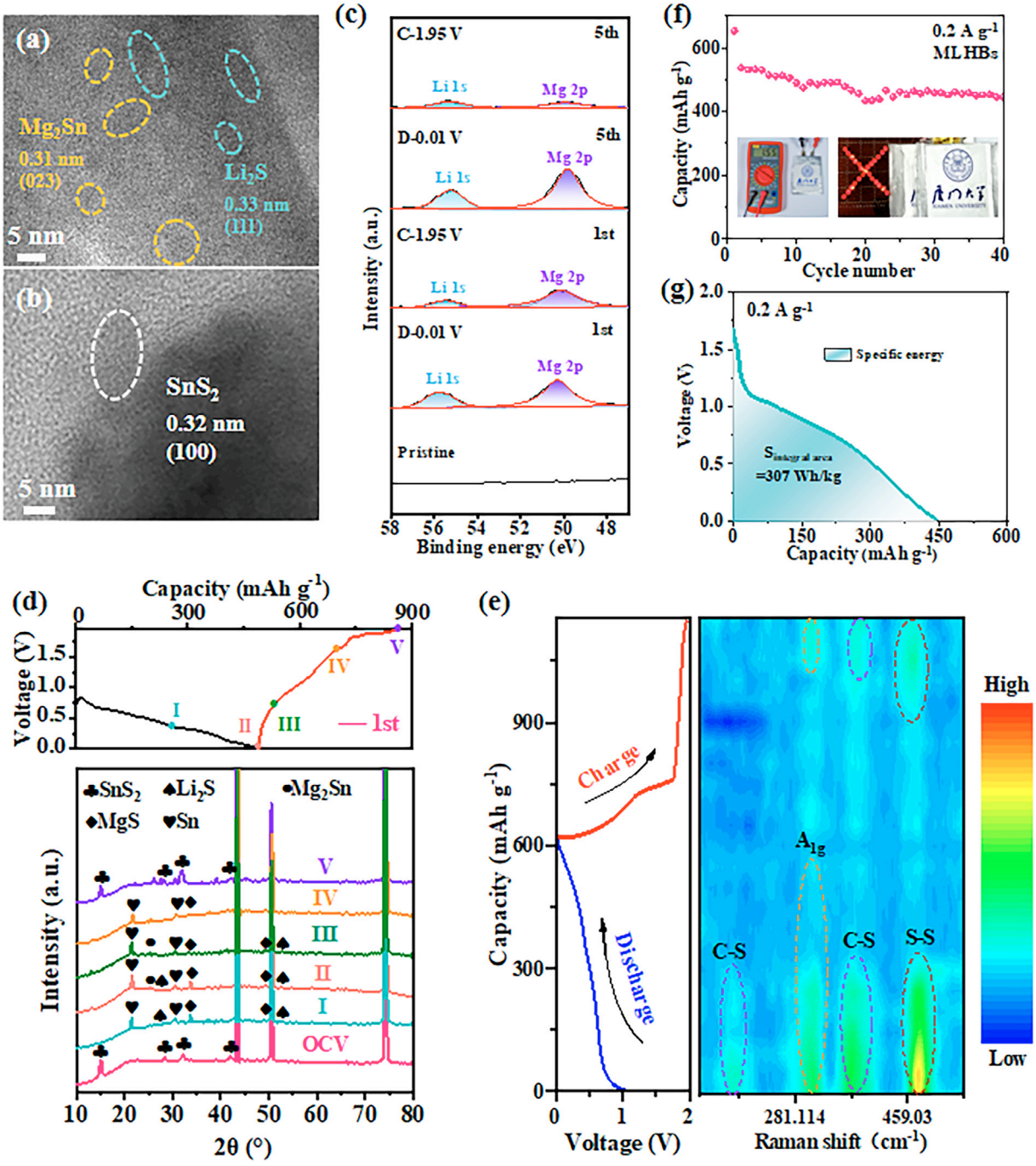

Fig. 4. Electrochemical reaction mechanism analysis of SnS_2-SPAN: HRTEM image after (a) discharging to 0.01 V and (b) charging to 1.95 V at the first cycle. (c) Ex-situ XPS spectra of Mg and Li signal after cycling one and five times, respectively. (d) The GCD profiles and ex-situ XRD at various cut-off voltages after cycling 1 time. (e) In-situ Raman spectra during 1st cycle. (f) Cycling performance of MLHB pouch cell at 0.2 A g^{-1} and (g) corresponding energy density calculated based on the mass of cathode active material.

occurrence of alloy reaction. During the following charging process (from state III to V), the peak intensities of SnS_2 are obviously enhanced and the peak at about 15 ° returns to the original position, demonstrating the good reversibility of conversion-alloy reactions and the superior structural stability of SnS_2-SPAN [33].

The in-situ Raman spectra of SnS_2-SPAN cathodes during 1st cycle is displayed in Fig. 4e, the results suggest that the SPAN is mainly involved in the reaction at high potential while SnS_2 is mainly involved in the reaction at low potential. There is no obvious change for the peak position, but the peak intensity changes significantly. Explicitly, during the discharge process, the peak intensities of the C–S and S–S bonds gradually weaken while that of the A_{1g} keeps almost unchanged at high potential, indicating that SPAN is mainly involved in the reaction.

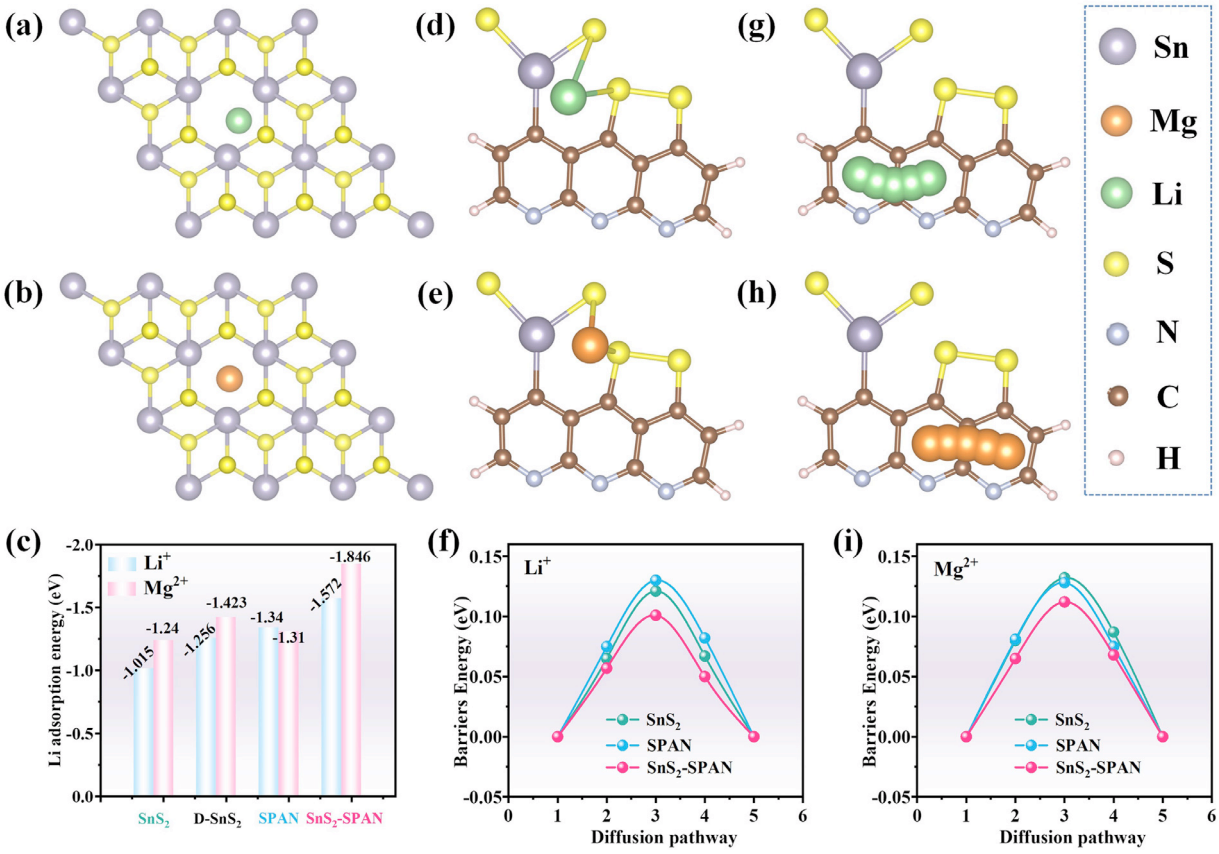

Fig. 5. DFT calculations: Optimized structures of (a) Li and (b) Mg absorbed on the S vacancy of SnS_2. (c) E_a of Li^+ and Mg^{2+} on the bulk SnS_2, the S vacancy of SnS_2, SPAN and SnS_2-SPAN. Optimized structures of (d) Li and (e) Mg absorbed on the SnS_2-SPAN. (f) Li^+ diffusion pathway and corresponding E_b on the bulk SnS_2, SPAN and SnS_2-SPAN. Illustration of the (g) Li^+ and (h) Mg^{2+} diffusion path in the SnS_2-SPAN. (i) Mg^{2+} diffusion pathway and corresponding E_b on the bulk SnS_2, SPAN and SnS_2-SPAN.

While the peak intensity of A_{1g} is obviously weakened at low potential, showing that SnS_2 is mainly involved in the reaction. This conclusion is consistent with CV analysis. Overall, the intensity of all peaks incrementally weakens during the discharge process and progressively recover again during the subsequent charge process, which are correlated with the insertion and extraction of Mg^{2+}/Li^+ into/from the SnS_2-SPAN.

To evaluate the practicability of SnS_2-SPAN electrode, SnS_2-SPAN//Mg pouch cell is prepared. As shown in the inset of Fig. 4f, the open circuit voltage of the pouch cell is as high as 1.55 V, and the two pouch cells in series can light up 25 LED lights. In Fig. 4f, the SnS_2-SPAN//Mg pouch cell delivers a high discharge capacity of 446 mAh g^{-1} at 0.2 A g^{-1} after cycling 40 times, accompanying with an energy density (based on the mass of cathode active material) up to 307 Wh kg^{-1} (Fig. 4g), which is one of the highest value among other cathode materials reported previously (Table S3). The corresponding GCD curves at 0.2 A g^{-1} are displayed in Fig. S27a, the discharge platform of the pouch cell has good consistency with the coin-type battery. Impressively, a high discharge capacity of 192 mAh g^{-1} after 500 cycles at 1 A g^{-1} can be achieved for the pouch cell (Fig. S27b). Satisfactory electrochemical performances of the SnS_2-SPAN//Mg pouch cell indicate the good practicability of SnS_2-SPAN cathode.

Encouraged by the excellent electrochemical performance of SnS_2-SPAN in MLHBs, density-functional theory (DFT) calculations are carried out to further explore the significance of the formed strong C–Sn bond and abundant S defects on the enhanced electrochemical performance. Fig. 5a and b display the optimized structures of Li and Mg absorbed on the S vacancy of SnS_2 (D-SnS_2), the adsorption energy (E_a) are −1.256 and −1.423 eV, respectively, which is larger than −1.015 (Li^+) and −1.24 eV (Mg^{2+}) for bulk SnS_2 (Fig. S28a and b), demonstrating the abundant S defects can supply more electrochemical active sites for Mg^{2+}/Li^+ co-intercalation and enhance the adsorption of cathode material for Mg^{2+} and Li^+. The E_a of Li^+ and Mg^{2+} on different samples are shown in Fig. 5c, wherein SnS_2-SPAN shows a stronger adsorption effect for Li^+ and Mg^{2+}, significantly better than the bulk SnS_2 and SPAN (Fig. 5d-e and Fig. S28), which can be attributed to the strong C–Sn bond formed in SnS_2-SPAN can effectively promote the charge transfer, and thus increase the adsorption energy of Li^+ and Mg^{2+}. To study the reaction kinetics, the diffusion energy barriers (E_b) of

Li^+ and Mg^{2+} in different samples are also calculated (Fig. 5g-h and Fig. S29). As exhibited in Fig. 5f and Fig. 5i, compared with SnS_2 and SPAN, SnS_2-SPAN with strong C–Sn bond displays a lower diffusion energy barrier, confirming the preferable Mg^{2+} and Li^+ diffusion kinetics. In summary, the DFT calculation results confirm that SnS_2-SPAN has the strongest Li^+/Mg^{2+} adsorption energy and fastest reaction kinetics than other samples due to the induced abundant sulfur vacancies and strong C–Sn bond.

3. Conclusion

In conclusion, a simple and versatile strategy has been proposed for synthesizing SnS_2 nanoparticles confined into 3D SPAN network, in which SPAN provides both physical and chemical dual-confinement for SnS_2. A series of in/ex-situ characterizations confirm the conversion-alloy mechanism and Mg^{2+}/Li^+ co-intercalation mechanism of SnS_2-SPAN cathode, simultaneously attesting to its preferable structural stability and reaction reversibility. DFT calculations indicate that the formed strong C–Sn bond and rich sulfur defects make the SnS_2-SPAN exhibit stronger Li^+/Mg^{2+} adsorption energy and faster reaction kinetics. As expected, the SnS_2-SPAN cathode exhibits high specific capacity and ultra-long cycling life in MLHBs. Additionally, satisfactory electrochemical performances and a high energy density (307 Wh kg^{-1}) of the SnS_2-SPAN//Mg pouch cell indicate the good practicability. This work provides a reference for the development of advanced cathode materials with Mg^{2+}/Li^+ co-intercalation for MLHBs.

Declaration of competing interest

In view of originality, significance, and broad interest, we feel that our new findings are worthy to be published in the journal of Journal of Magnesium and Alloys. We claim here that none of the results have been published or submitted elsewhere. According to policy as well as my moral obligation, as the researchers report I am a consultant from a company in financial and/or commercial interests. May be limited by the attached paper reports the research. I have been to Taylor and Francis fully revealed these interests, and I have worked out a plan for approval to manage any potential conflicts caused by the participation.

CRediT authorship contribution statement

Yiyi Wang: Writing – review & editing, Writing – original draft, Investigation, Formal analysis, Data curation, Conceptualization. **Zhenfeng Guan:** Writing – review & editing, Formal analysis, Data curation. **Yinggan Zhang:** Writing – review & editing, Software, Resources. **Baihua Qu:** Writing – review & editing, Writing – original draft, Supervision, Formal analysis, Data curation, Conceptualization. **Baisheng Sa:** Software, Resources. **Xiaoyuan Zhou:** Supervision, Project administration, Funding acquisition. **Jingfeng Wang:** Writing – review & editing, Validation, Funding acquisition. **Dong-Liang Peng:** Writing – review & editing, Writing – original draft, Supervision, Project administration, Formal analysis, Data curation, Conceptualization. **Qingshui Xie:** Writing – review & editing, Writing – original draft, Supervision, Project administration, Funding acquisition, Formal analysis, Data curation, Conceptualization. **Fusheng Pan:** Writing – review & editing, Supervision, Project administration.

Acknowledgments

This work was financially supported by the National Key R&D Program of China (No. 2023YFB3809500), National Natural Science Foundation of China (Grant No. 51931006, 52272240 and U22A20118), the Fundamental Research Funds for the Central Universities of China (Xiamen University: No. 20720220074), Science and Technology Projects of Innovation Laboratory for Sciences and Technologies of Energy Materials of Fujian Province (HRTP-[2022]−22) and the "Double-First Class" Foundation of Materials Intelligent Manufacturing Discipline of Xiamen University.

Supplementary materials

Supplementary material associated with this article can be found, in the online version, at doi:10.1016/j.jma.2024.11.025.

References

[1] J.B. Goodenough, Y. Kim, Chem Mater 22 (3) (2010) 587–603.
[2] X.B. Cheng, R. Zhang, C.Z. Zhao, Q. Zhang, Chem Rev 117 (15) (2017) 10403–10473.
[3] Y.W. Chen, M.H. Li, Y. Liu, Y.L. Jie, W.X. Li, F.Y. Huang, X.P. Li, Z.X. He, X.D. Ren, Y.H. Chen, X.H. Meng, T. Cheng, M. Gu, S.H. Jiao, R.G. Cao, Nat Commun 14 (1) (2023) 2655.
[4] Z.J. Huang, J.C. Lai, S.L. Liao, Z. Yu, Y.L. Chen, W.L. Yu, H.X. Gong, X. Gao, Y.F. Yang, J. Qin, Y. Cui, Z.A. Bao, Nat Energy 8 (6) (2023) 577–585.
[5] J.W. Huang, K. Wu, G. Xu, M.H. Wu, S.X. Dou, C. Wu, Chem Soc Rev 52 (15) (2023) 4933–4995.
[6] W. Liu, P.C. Liu, D. Mitlin, Chem Soc Rev 49 (20) (2020) 7284–7300.
[7] C.L. Wei, L.W. Tan, Y.C. Zhang, B.J. Xi, S.L. Xiong, J.K. Feng, Y.T. Qian, Energy Stroage Mater 48 (2022) 447–457.
[8] S.Y. Hou, X. Ji, K. Gaskell, P.F. Wang, L.N. Wang, J.J. Xu, R.M. Sun, O. Borodin, C.S. Wang, Science 374 (6564) (2021) 172–178.
[9] H. Dong, O. Tutusaus, Y.L. Liang, Y. Zhang, Z. Lebens-Higgins, W.L. Yang, R. Mohtadi, Y. Yao, Nat Energy 5 (12) (2020) 1043–1050.
[10] Y. Liu, B. Qu, S. Li, X. Lian, Y. Luo, X. Shen, C. Xu, J. Wang, F. Pan, Adv Funct Mater 34 (2024) 2405586.
[11] L. Zhou, C. Shen, X. Hou, Z. Fang, T. Jin, K. Xie, J Magnes Alloy 12 (5) (2024) 1830.
[12] F.F. Liu, T.T. Wang, X.B. Liu, L.Z. Fan, Adv. Energy Mater 11 (2) (2021) 2000787.
[13] C. Wang, Y. Huang, Y. Lu, H. Pan, B.B. Xu, W. Sun, M. Yan, Y. Jiang, Nano-Micro Lett 13 (2021) 195.
[14] T. Wen, Y. Deng, B. Qu, G. Huang, J. Song, C. Xu, A. Du, Q. Xie, J. Wang, G. Cui, D.-L. Peng, X. Zhou, F. Pan, ACS Energy Lett 8 (2023) 4848.

[15] D. Aurbach, Z. Lu, A. Schechter, Y. Gofer, H. Gizbar, R. Turgeman, Y. Cohen, M. Moshkovich, E. Levi, Nature 407 (6805) (2000) 724–727.
[16] H.D. Yoo, Y.L. Liang, H. Dong, J.H. Lin, H. Wang, Y.S. Liu, L. Ma, T.P. Wu, Y.F. Li, Q. Ru, Y. Jing, Q.Y. An, W. Zhou, J.H. Guo, J. Lu, S.T. Pantelides, X.F. Qian, Y. Yao, Nat Commun 8 (2017) 339.
[17] Y.R. Wang, C.X. Wang, X. Yi, Y. Hu, L. Wang, L.B. Ma, G.Y. Zhu, T. Chen, Z. Jin, Energy Storage Mater 23 (2019) 741–748.
[18] M. Rashad, M. Asif, Y.X. Wang, Z. He, I. Ahmed, Energy Storage Mater 25 (2020) 342–375.
[19] P.Y. Wang, X.B. Yan, Energy Storage Mater 45 (2022) 142–181.
[20] G.L. Zhu, G.L. Xia, H.G. Pan, X.B. Yu, Adv Sci 9 (13) (2022).
[21] X. Xu, C. Ye, D.L. Chao, K. Davey, S.Z. Qiao, Adv Energy Mater 13 (12) (2023) 2204344.
[22] X.B. Yu, G.Y. Zhao, C. Liu, C.L. Wu, H.H. Huang, J.J. He, N.Q. Zhang, Adv Funct Mater 31 (42) (2021) 2103214.
[23] H. Xu, X. Zhang, T. Xie, Z. Li, F.Z. Sun, N. Zhang, H.Y. Chen, Y.X. Zhu, X.S. Zou, C. Lu, J.X. Zou, R.M. Laine, Energy Storage Mater 46 (2022) 583–593.
[24] Y.N. Xu, X.W. Deng, Q.D. Li, G.B. Zhang, F.Y. Xiong, S.S. Tan, Q.L. Wei, J. Lu, J.T. Li, Q.Y. An, L.Q. Mai, Chem 5 (5) (2019) 1194–1209.
[25] X.L. Xue, R.P. Chen, C.Z. Yan, P.Y. Zhao, Y. Hu, W.H. Kong, H.N. Lin, L. Wang, Z. Jin, Adv Energy Mater 9 (22) (2019) 1900145.
[26] R.M. Sun, C.Y. Pei, J.Z. Sheng, D.D. Wang, L. Wu, S.J. Liu, Q.Y. An, L.Q. Mai, Energy Storage Mater 12 (2018) 61–68.
[27] H. Xu, Y. Li, D. Zhu, Z. Li, F.Z. Sun, W. Zhu, Y. Chen, J.C. Zhang, L. Ren, S.H. Zhang, J.X. Zou, R.M. Laine, Adv Energy Mater 12 (38) (2022) 2201608.
[28] X. Fan, M. Tebyetekerwa, Y.L. Wu, R.R. Gaddam, X.S. Zhao, Nano-Micro Lett 14 (1) (2022) 177.
[29] Y.Y. Shan, Y. Li, H. Pang, Adv Funct Mater 30 (23) (2020) 2001298.
[30] C.H. Wu, G.J. Zhu, Q. Wang, M.H. Wu, H.J. Zhang, Energy Storage Mater 43 (2021) 430–462.
[31] Y.Y. Wang, J.B. Liu, X.C. Chen, B.Y. Kang, H.E. Wang, P.X. Xiong, Q.H. Chen, M.D. Wei, N. Li, Q.R. Qian, L.X. Zeng, Carbon N Y 189 (2022) 46–56.
[32] Y.Y. Wang, X. Chen, X.C. Chen, C.Y. Lin, H.E. Wang, P.X. Xiong, Q.H. Chen, Q.R. Qian, M.D. Wei, L.X. Zeng, J Mater Chem A 10 (21) (2022) 11449–11457.
[33] Y.Y. Wang, F.Y. Xiao, X. Chen, P.X. Xiong, C.Y. Lin, H.E. Wang, M.D. Wei, Q.R. Qian, Q.H. Chen, L.X. Zeng, Infomat 5 (9) (2023).
[34] J. Yuan, B. Yu, D. Pan, X. Hu, J.X. Chen, M. Aminua, Y.J. Liu, L.M. Sheng, Y.H. Chen, Y.M. Wu, H.B. Zhan, Z.H. Wen, Adv Funct Mater 33 (46) (2023) 2305503.
[35] W.R. Tian, J. Han, L.C. Wan, N.J. Li, D.Y. Chen, Q.F. Xu, H. Li, J.M. Lu, Nano Energy 107 (2023).
[36] Y.Q. Zhang, L. Tao, C. Xie, D.D. Wang, Y.Q. Zou, R. Chen, Y.Y. Wang, C.K. Jia, S.Y. Wang, Adv Mater 32 (7) (2020) 1905923.
[37] S. Wang, B.Y. Lu, D.Y. Cheng, Z.H. Wu, S.J. Feng, M.H. Zhang, W.K. Li, Q.S. Miao, M. Patel, J.Q. Feng, E. Hopkins, J.B. Zhou, S. Parab, B. Bhamwala, B. Liaw, Y.S. Meng, P. Liu, J Am Chem Soc 145 (17) (2023) 9624–9633.
[38] X. Chen, L.F. Peng, L.H. Wang, J.Q. Yang, Z.X. Hao, J.W. Xiang, K. Yuan, Y.H. Huang, B. Shan, L.X. Yuan, J. Xie, Nat Commun 10 (2019).
[39] Y.Z. Huang, Y.X. Ji, L.X. Zhang, C.Y. Cai, Y. Fu, Adv Funct Mater 33 (44) (2023) 2306484.
[40] C.L. Du, Y.Q. Zhu, Y.X. Zhang, H. Peng, J.C. Tian, T.Y. Xia, L.F. Yang, X. Liu, X.L. Ma, C.B. Cao, Energy Storage Mater 61 (2023) 102863.
[41] F.Q. Luo, X.S. Feng, L.X. Zeng, L.X. Lin, X.Y. Li, B.Y. Kang, L.R. Xiao, Q.H. Chen, M.D. Wei, Q.R. Qian, Chem Eng J 404 (2021) 126430.
[42] X. Hu, M. Qiu, Y.J. Liu, J. Yuan, J.X. Chen, H.B. Zhan, Z.H. Wen, Adv Energy Mater 12 (47) (2022) 2202318.
[43] Y.J. Liu, M. Qiu, X. Hu, J. Yuan, W.L. Liao, L.M. Sheng, Y.H. Chen, Y.M. Wu, H.B. Zhan, Z.H. Wen, Nano-Micro Lett 15 (1) (2023) 104.
[44] X.Y. Yang, C.L. Du, Y.Q. Zhu, H. Peng, B.L. Liu, Y.H. Cao, Y.X. Zhang, X.L. Ma, C.B. Cao, Chem Eng J 430 (2022) 133108.
[45] Y. Li, Y.H. Xu, Z.H. Wang, Y. Bai, K. Zhang, R.Q. Dong, Y.N. Gao, Q. Ni, F. Wu, Y.J. Liu, C.A. Wu, Adv Energy Mater 8 (23) (2018) 1800927.
[46] W. Zhong, S.W. Li, M.C. Liu, Z.Q. Zeng, S.J. Cheng, J. Xie, Nano Energy 115 (2023) 108757.
[47] W. Yao, J.M. Chen, Y.J. Wang, R.Q. Fang, Z. Qin, X.F. Yang, L.Y. Chen, Y.W. Li, Angew Chem Int Ed 60 (44) (2021) 23729–23734.
[48] X.J. Hou, H.C. Shi, T.J. Chang, K.M. Hou, L. Feng, G.Q. Suo, X.H. Ye, L. Zhang, Y.L. Yang, W. Wang, Chem Eng J 409 (2021) 128271.
[49] T. Ma, Y.X. Ni, D.T. Li, Z.T. Zha, S. Jin, W.J. Zhang, L.Q. Jia, Q. Sun, W.W. Xie, Z.L. Tao, J. Chen, Angew Chem Int Ed 62 (43) (2023).
[50] J.T. Zai, X.F. Qian, K.X. Wang, C. Yu, L.Q. Tao, Y.L. Xiao, J.S. Chen, Crystengcomm 14 (4) (2012) 1364–1375.
[51] Z.T. Wang, Y.Q. Zhu, C. Qiao, S. Yang, J. Jia, S. Rafai, X.L. Ma, S.D. Wu, F.Q. Ji, C.B. Cao, Small 15 (42) (2019) 1902797.
[52] X. Liu, Y.Q. Zhu, C.L. Du, J.C. Tian, L.F. Yang, X.Y. Yao, Z.T. Wang, X.L. Ma, J.H. Hou, C.B. Cao, Chem Eng J 463 (2023).
[53] X. Fan, R.R. Gaddam, N.A. Kumar, X.S. Zhao, Adv. Energy Mater 7 (19) (2017) 1700317.
[54] Y.L. Zhang, Y. Li, Y. Wang, R. Guo, W. Liu, H.J. Pei, G.P. Yin, D.X. Ye, S.X. Yu, J.Y. Xie, J Colloid Interface Sci 553 (2019) 239–246.
[55] N. Wu, Z.Z. Yang, H.R. Yao, Y.X. Yin, L. Gu, Y.G. Guo, Angew Chem Int Ed 54 (19) (2015) 5757–5761.
[56] Y. Meng, Y.Y. Zhao, D.S. Wang, D. Yang, Y. Gao, R.Q. Lian, G. Chen, Y.J. Wei, J Mater Chem A 6 (14) (2018) 5782–5788.
[57] C.Y. Pei, F.Y. Xiong, J.Z. Sheng, Y.M. Yin, S.S. Tan, D.D. Wang, C.H. Hang, Q.Y. An, L.Q. Mai, ACS Appl Mater Interfaces 9 (20) (2017) 17061–17067.
[58] J. Tian, D.P. Cao, X.J. Zhou, J.L. Hu, M.S. Huang, C.L. Li, ACS Nano 12 (4) (2018) 3424–3435.
[59] S.Q. Ding, X. Dai, Y.X. Tian, G.Y. Song, Z.J. Li, A. Meng, L. Wang, G.C. Li, W.J. Wang, J.F. Huang, S.X. Li, ACS Appl Mater Interfaces 13 (45) (2021) 54005–54017.
[60] R.R. Deng, S.S. Tan, Z.T. Wang, R. Li, G.J. Lu, B.H. Qu, L. Tong, R.H. Wang, C.H. Xu, G.S. Huang, J.F. Wang, A.T. Tang, X.Y. Zhou, F.S. Pan, ACS Appl Mater Interfaces 15 (23) (2023) 27984–27994.
[61] Y.H. Cao, Y.Q. Zhu, C.L. Du, X.Y. Yang, T.Y. Xia, X.L. Ma, C.B. Cao, ACS Nano 16 (1) (2022) 1578–1588.
[62] Y. Xu, G.L. Fan, P.X. Sun, Y. Guo, Y.Y. Wang, X.J. Gu, L.M. Wu, L. Yu, Angew Chem Int Ed 62 (26) (2023) e202303529.
[63] X.J. Pu, D. Zhao, C.L. Fu, Z.X. Chen, S.A. Cao, C.S. Wang, Y.L. Cao, Angew Chem Int Ed 60 (39) (2021) 21310–21318.
[64] Y.Y. Ding, T.L. Han, Z. Wu, Y. Guan, J. Hu, C.Q. Hu, Y.C. Tian, J.Y. Liu, ACS Nano 16 (9) (2022) 15369–15381.
[65] Z.S. Ye, P. Li, W.T. Wei, C. Huang, L.W. Mi, J.L. Zhang, J.J. Zhang, Adv Sci 9 (18) (2022) 2200067.
[66] Y.R. Wang, Z.T. Liu, C.X. Wang, X. Yi, R.P. Chen, L.B. Ma, Y. Hu, G.Y. Zhu, T. Chen, Z.X. Tie, J. Ma, J. Liu, Z. Jin, Adv Mater 30 (32) (2018) 1802563.
[67] S.Q. Ding, X. Dai, Z.J. Li, C.S. Wang, A. Meng, L. Wang, G.C. Li, J.F. Huang, S.X. Li, Energy Storage Mater 47 (2022) 211–222.
[68] W.Q. Yao, C.X. Tian, C. Yang, J. Xu, Y.F. Meng, I. Manke, N. Chen, Z.L. Wu, L. Zhan, Y.L. Wang, R.J. Chen, Adv Mater 34 (11) (2022) 2106370.
[69] T. Gao, S. Hou, F. Wang, Z.H. Ma, X.G. Li, K. Xu, C.S. Wang, Angew Chem Int Ed 56 (43) (2017) 13526–13530.
[70] T. Luo, Y. Wang, B. Elander, M. Goldstein, Y. Mu, J. Wilkes, M. Fahrenbruch, J. Lee, T. Li, J.L. Bao, U. Mohanty, D. Wang, Adv Mater 36 (7) (2023) 2306239.